

# A multidisciplinary approach to structural health monitoring and damage prognosis of aerospace hotspots

**A. Chattopadhyay**

**P. Peralta**

Department of Mechanical and Aerospace Engineering  
Arizona State University  
Tempe, Arizona  
USA

**A. Papandreou-Suppappola**

**N. Kovvali**

**papandreou@asu.edu**      **narayan.kovvali@asu.edu**  
Department of Electrical Engineering  
Arizona State University  
Tempe, Arizona  
USA

## ABSTRACT

The health monitoring and damage prognosis of aerospace hotspots is important for reducing maintenance costs and increasing in-service capacity of aging aircraft. One of the leading causes of structural failure in aerospace vehicles is fatigue damage. Based on the physical mechanism of damage nucleation and growth, a physics-based multiscale model is considered for fatigue damage assessment in metallic aircraft structures. A guided-wave based sensing approach is utilised to enable effective damage detection in a common structural hotspot: a lug joint. Finite element analysis is carried out with piezoelectric wafers bonded to the host structure and the simulated sensor signals are analysed. A damage classification strategy is developed, which integrates physically motivated time-frequency approaches with advanced stochastic modelling techniques. In particular, a variational Bayesian learning scheme is used to estimate the optimal model complexity automatically from the data, adapting the classifier for real-time use. Classification performance is studied as a function of signal-to-noise ratio and results are reported for the detection of fatigue crack damage in the lug joint. An adaptive hybrid prognosis model is proposed, which estimates the residual useful life of structural hotspots using damage condition information obtained in real-time.

## NOMENCLATURE

$\mathbf{A}$	state-transition matrix
$B$	state-dependent observation density
$E_{s_k}$	MPD-TFR of $s_k$
$f$	frequency
$F_N$	variational objective function
$g_k$	$k$ th atom in MPD
$K$	number of MPD iterations
$L$	fatigue cycle
$M$	number of damage classes
$N$	number of HMM states
$N^*$	optimal number of HMM states
$p_{ij}$	$(i, j)$ th entry of confusion matrix
$R_k$	residue after $K$ MPD iterations
$s$	time-domain signal
$s_K$	$K$ -term MPD approximation to $s$
$t$	time
$T$	length of observation sequences
$WD_{g_k}$	Wigner distribution of $g_k$
$x$	state sequence
$x_n$	state at time $n$
$y$	observation sequence

$y_n$	observation at time $n$
$\alpha_k$	$k$ th expansion coefficient in MPD
$\tau_k$	$k$ th time-shift
$\nu_k$	$k$ th frequency-shift
$\kappa_k$	$k$ th scale
$\pi$	initial state distribution
$\theta$	HMM parameter set
$\theta_{ML}$	maximum-likelihood estimate of $\theta$

## 1.0 INTRODUCTION

The ability to effectively model, detect, classify, and predict damage in complex airframe structures is an important problem in the area of structural health monitoring (SHM)<sup>(1-3)</sup>. In this regard, one of the leading causes of structural failure in aerospace vehicles is fatigue damage. Although significant attention has been devoted to this subject in recent years, prediction of the failure modes associated with fatigue damage still remains a challenging area of research<sup>(4)</sup>. This paper presents a multidisciplinary approach to the SHM and damage prognosis of aerospace hotspots.

Traditional life prediction methods are mainly based on macroscopic response of material behavior and the failure laws mostly depend on experimental observations. In this work, a physics-based multiscale model is considered for fatigue damage assessment. From the physical point of view, microcracks in a metallic component initiate at the microscale, often at the surface of the material. This is Stage I cracking, where microcracks are inside individual grains and tend to follow crystallographic planes with high shear stress. Then follows Stage II, in which the microcracks cross the crystal boundaries to grow more or less perpendicular to the direction of the maximum principal stress up to coalescence to produce a mesocrack<sup>(5)</sup>. This physical mechanism forms the basis of our multiscale modelling approach.

A guided-wave propagation study<sup>(6-9)</sup> is conducted on lug joints, which represent a typical structural hotspot. Guided-waves have demonstrated potential in monitoring large areas of metallic aircraft fuselage<sup>(10)</sup>. Finite element analysis is carried out with piezoelectric wafers bonded to the host structure. Piezoelectric sensors/actuators are of particular interest due to the need for onboard SHM. Simulation of sensor signals is performed accounting for the two-way piezoelectrical-mechanical coupling.

A broad range of signal analysis methodologies have been proposed to date for damage detection and classification. Examples include Lamb wave methods<sup>(11)</sup>, multi-resolution wavelet transforms<sup>(12)</sup>, impedance-based approaches<sup>(13)</sup>, statistical pattern recognition techniques using outlier analysis<sup>(14)</sup>, and artificial neural networks<sup>(15)</sup>. While the physics-based deterministic methods work well in controlled situations, they are not robust to the variability prevalent in real-world scenarios. For example, the data measured using sensors can be strongly influenced by changes in environmental or operation conditions, sensor characteristics and malfunctions, etc. Statistical approaches account for this uncertainty, and when combined with the physically motivated analysis, lead to reliable damage identification systems. In this work, a damage classification strategy is presented that integrates a physically motivated signal analysis framework — namely, time-frequency analysis<sup>(16-18)</sup> — with advanced stochastic modeling techniques. The primary benefit of the joint time-frequency analysis procedure over standard time-domain or Fourier techniques is that it is better suited to explore the dispersive or time-varying phenomena characteristic of material wave-physics. By capturing the essentials of the non-stationary structure of the signals of interest in the SHM problem, time-frequency analysis results in a more informative framework for damage identification. Also described here is the use of a variational Bayesian learning scheme to estimate the optimal model complexity automatically from the data in order to adapt the classifier for real-time use.

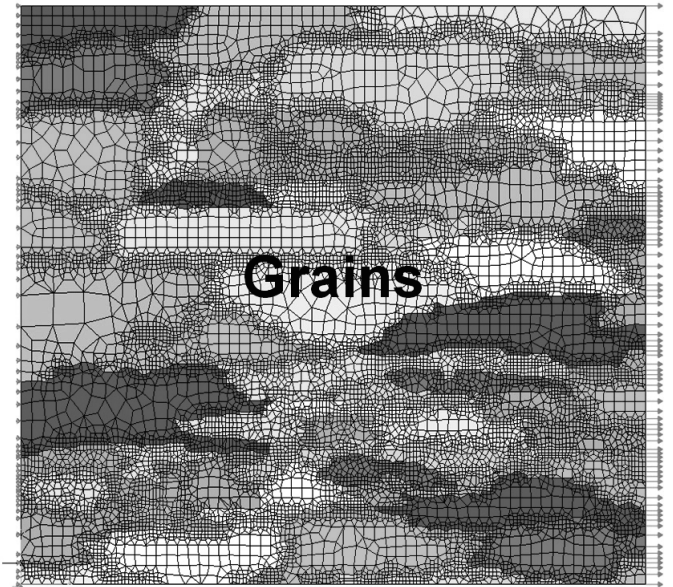


Figure 1. FEA model.

Current aerospace practice follows an engineering model based on damage-tolerant reliability wherein structural components are regularly inspected and replaced. In this scheme, engineering designs are generally based on a physics-based fracture mechanics approach in which the life of structural component is estimated using an assumed initial damaged condition. However, in a real-time environment, keeping track of the damage condition of a complex structural component manually is quite difficult and requires automatic damage state estimation. The real-time damage state information should be regularly fed to a prognosis model to update the residual useful life estimation in the event of a new prevailing situation. In the present paper, the use of an adaptive hybrid prognosis model is discussed that estimates the residual useful life of a structural hotspot using information on the damage condition obtained in real-time. The hybrid prognosis model has two modules: an offline prognosis module that forecasts the future damage state, and an online state estimation module which regularly predicts the current damage state and feeds into the offline module in real-time. This estimation can be carried out using online sensor data acquisition coupled with the time-frequency analysis mentioned above. Both the offline and online modules are probabilistic models and use the concept of Bayesian inference based on input-output mapping through a Gaussian process.

The remainder of the paper is organised as follows. In Section 2, the physics-based multiscale model is developed for fatigue damage assessment. Section 3 deals with the damage detection approach for the lug joint. In Section 4, damage classification techniques based on time-frequency analysis are described and results are provided for classifying crack damage in a lug joint. The algorithm's performance is also analysed in the presence of noise. Section 5 discusses the hybrid prognosis model based on physics and data driven techniques. This is followed by concluding remarks in Section 6.

## 2.0 PHYSICALLY BASED MULTISCALE MODELLING

The need to predict the evolution of fatigue damage from crack nucleation to long crack propagation requires a physics-based multiscale model. A multiscale model that accounts for grain orientation effects is developed to capture the damage initiation and progression due to high cycle fatigue (HCF). To implement the micro-meso multiscale model into the application for HCF, a corresponding modified fatigue damage criterion is also used<sup>(19)</sup>.

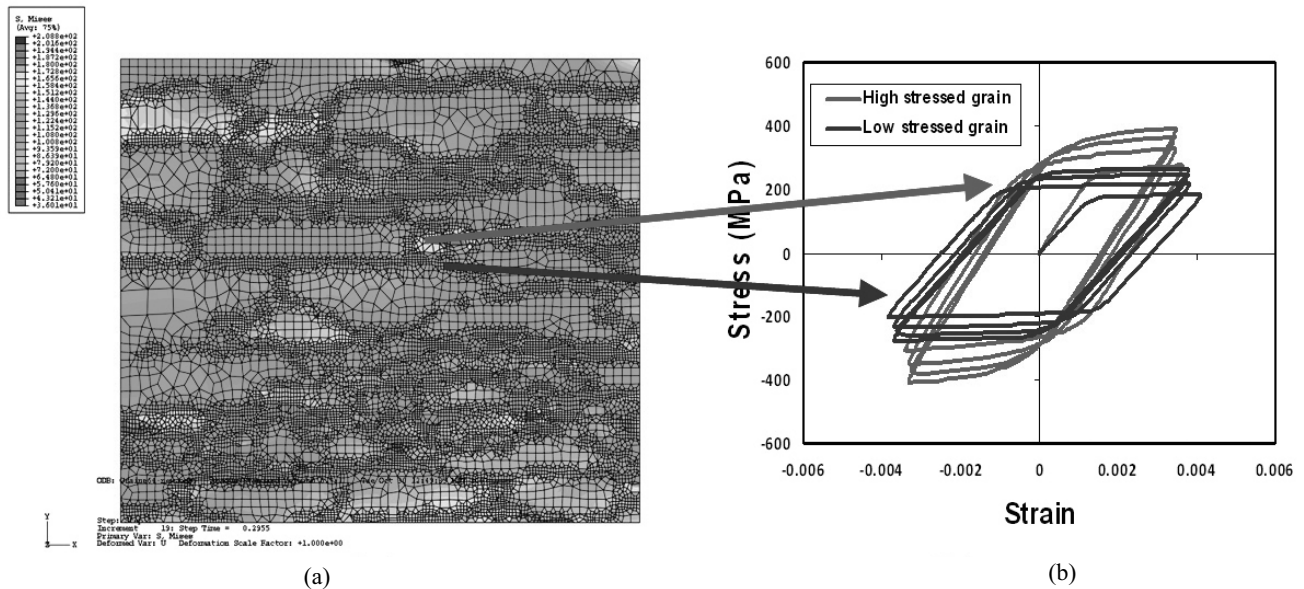


Figure 2. (a) Mises stress distribution, (b) Stress-strain response in different grains.

## 2.1 Approach

The present approach differs from classical mathematical homogenisation in two ways: (i) the local fields are allowed to deviate from the average condition determined by the effective material properties by accounting for local microstructural features, and (ii) micro-, meso- and macroscale modelling are linked to approximate fatigue damage accumulation and failure response. Electron backscatter diffraction (EBSD) is used to obtain the crystallographic orientation for each grain in the critical location, and these orientations, in turn, are used to assign appropriate material properties to each grain. The region surrounding the critical location is treated as a homogeneous material with properties given by the average response of an appropriately sized representative region at the microscale. The boundary condition at the interface (between the critical location and the surrounding region) and the grain size and grain orientation together determine the stress and strain distribution within the critical site. The representative structure is described using local representative volume elements (RVEs) at the microscale and the mesoscale, respectively.

Single crystal plasticity<sup>(20–25)</sup> is used to capture crystallographic orientation effects that are not considered by classical isotropic models of metal plasticity. Only face-centred cubic (FCC) crystalline material is considered in this paper. A FCC crystal has four slip planes and each slip plane has three slip directions, resulting in 12 slip systems. In order to reflect fatigue hardening and saturation phenomenon, a nonlinear Armstrong-Frederick type of kinematic hardening is applied. The microscale model is implemented within a commercially available software package (ABAQUS) through an implicit material subroutine (UMAT). The single crystal plasticity applied at the micro level is also implemented at the meso level. In this model, the original microstructure contained 547 grains, which is sufficient to define a RVE. This is reduced to 64 grains by combining smaller grains with larger or similar ones, ensuring computational efficiency. These small grains were chosen using a heuristic approach based upon the relative size and orientation of nearby grains; this ensures that no significant effects were excluded. Each grain is a single crystal that is modelled through the microscale analysis.

Fatigue simulation at the mesoscale comprises three steps. First, EBSD scans (Fig. 1) are used to determine the crystal orientations in terms of three Euler angles<sup>(19)</sup>. Second, the software package OOF (Object-Oriented Finite element analysis from NIST) is used to create and mesh the mesoscale structure from the EBSD scan. Grains are represented by various colours and each has the same material but different crystal orientation. Third, the commercial FEA

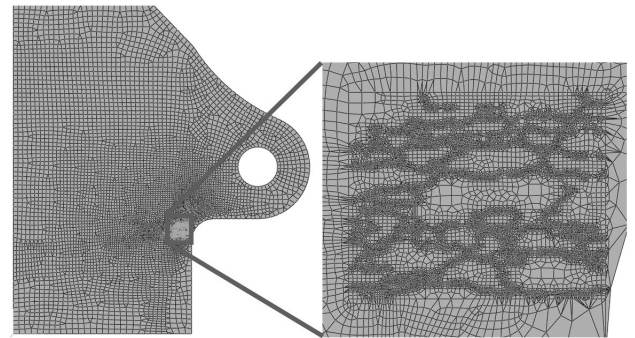


Figure 3. FE mesh of lug joint.

software ABAQUS and the previously developed UMAT are used to obtain stress distributions and the stress-strain response for any grain, as shown in Fig. 2. A cyclic displacement is applied at the right edge of the mesoscale structure. The Mises stress distribution and the stress-strain responses in different grains are presented in Fig 2. In Fig 2(a), the cool coloured grains (green and cooler) are still under elastic deformation while the warm coloured grains (yellow and red) already have plastic deformation. This indicates that material has an anisotropic heterogeneous response at the grain level due to different crystal orientations and grain shapes. The stress-strain response of two adjacent grains is plotted in Fig 2(b). These results support the conclusion that the material is anisotropic at this level and that differences in material response due to this anisotropy lead to local stress concentrations.

To illustrate the effect of the multiscale modelling, the meso RVE is used to model the high stress concentration zone in a structural component, i.e., a lug joint. The remaining portion of this lug joint is described as a homogeneous material. The finite element mesh and Mises stress distribution of the lug joint are shown in Figs 3 and 4. Figure 4 shows that inside the high stress concentration zone, there are regions of high stress closer to the free edge, due to different crystal orientations and microstructural geometry.

A physically based fatigue damage model<sup>(26)</sup> relating the damage to local stresses and strains at certain material planes has been modified for single crystal plasticity at the microscale. The concept

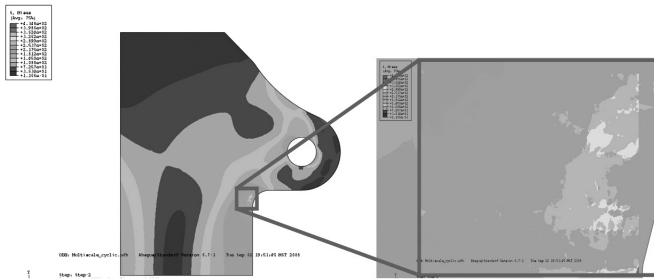


Figure 4. Mises stress distribution of lug joint.

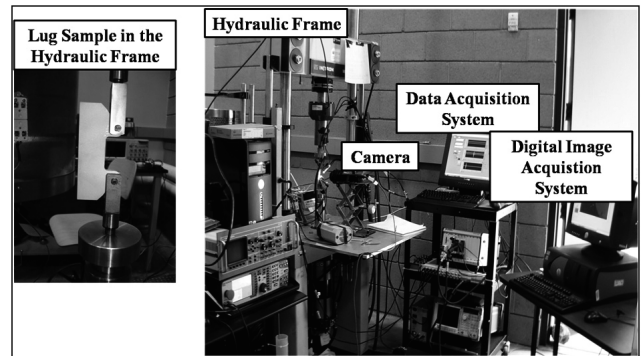


Figure 6. Experimental setup of the fatigue tests for lug joint samples.

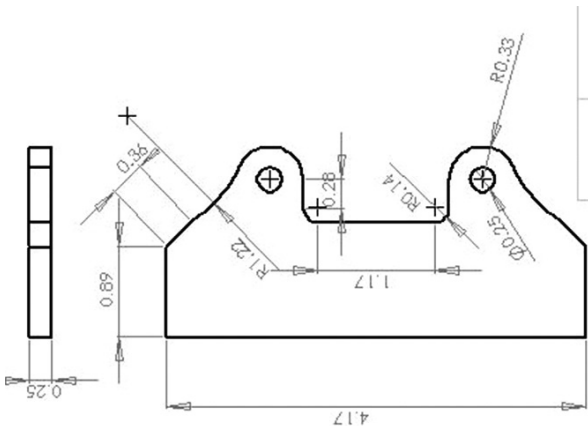


Figure 5. Geometrical dimensions of the lug joint sample.

of memory stress, which equals the maximum Mises equivalent stress, is used to control damage evolution. If the memory stress is less than the endurance limit, which can be regarded as a 'zero-damage' level, of the material, there is no damage growth. Once there is damage growth, the damage increment on certain material plane is related to the plastic strain energy density on the same plane. This allows tracking damage accumulation as a result of local plastic deformation, which is key for proper modelling of fatigue behaviour.

### 3.0 DAMAGE DETECTION IN STRUCTURAL HOTSPOTS

An important structural hotspot in which damage initiates and progresses under fatigue loading is the lug joint. An early detection of fatigue cracks in lug joints can help in taking preventive measures thus avoiding any possible structural failure. In this section, the focus is on detecting damage in this test article.

The lug joint samples were prepared from an Al 2024 T351 alloy plate with thickness of 6.35mm (0.25in). The dimensions of the lug joint sample are shown in Fig. 5.

To study the effect of surface finish, the lug joint samples were given two different surface finishes. Some of the samples were polished with silicon carbide paper to 1,200 grit (5 microns) while the surfaces of the remaining samples were sand blasted.

#### 3.1 Lug joint experiments — Fatigue tests

The lug was fatigued in an Instron 1331 servo-hydraulic load frame. Figure 6 shows the experimental setup. Pictures from a CCD camera were collected using a digital image acquisition system to monitor

Table 1  
Fatigue lives of the lug joint samples

Specimen	Constant amplitude fatigue loading	Fatigue life (no. of cycles)
Polished	(110lb – 1,100lb)	380,621
Sand blasted	(110lb – 1,100lb)	823,537
Sand blasted	(80lb – 800lb)	> 3m

potential locations for crack nucleation and measure crack length. Constant amplitude tensile loading was applied on the sample through pins passing through the pin holes. The clevis at the top is fixed whereas the one at the bottom is connected to the hydraulic actuator, where load is induced at a frequency of 20Hz using a sinusoidal waveform. Table 1 shows the fatigue life for the lug samples. It is observed that under the same applied loading of 490N (110lb) to 4,900N (1,100lb), the polished samples failed at much lower number of cycles as compared to the sand blasted ones. The failure modes of the lug joint samples are shown in Fig. 7. It can be seen that there were two distinct sites for crack initiation in the sample, one starting from the pin hole and the other at the shoulder of the lug. These two crack initiation sites were visible for the sand blasted lug sample shown in Fig. 7(b). However, as can be seen in Fig. 7, both samples failed at the same location when tested at the same load. In the case of a sand blasted sample subjected to a lower fatigue load, 356N (80lb) to 3,560N (800lb), the fatigue life increased significantly and the failure occurred due to crack growth from the pin hole.

This failure mode is shown in Fig. 7(c). The experimental results indicate that the type of surface finish not only influences the life of the sample but also changes the failure mode and location for different load amplitudes.

#### 3.2 Damage detection

From the fatigue tests conducted on the lug joint samples, it was observed that they failed at the shoulders under constant amplitude loading of (110lb to 1,100lb). Based on this observation, electrical discharge machining (EDM) notches of length 2mm and 4mm were made in the lug samples at that particular location. Three piezoelectric sensors and one actuator (APC 850) were glued to the surface around the notches while two more sensors were placed along the thickness direction. The sensor-actuator configuration is shown in Fig 8(a). The sensors/actuator network is intuitive and the sensitivity study presented in this paper helps to characterise damage. Sensor signals were acquired from the damaged sample and the undamaged sample, and those for the undamaged case were used as reference. A 4-5 cycles, 130KHz tone burst (Fig 8(b)) was used as the excitation signal. Signals were collected from all the sensors at a sampling rate of 2MHz.

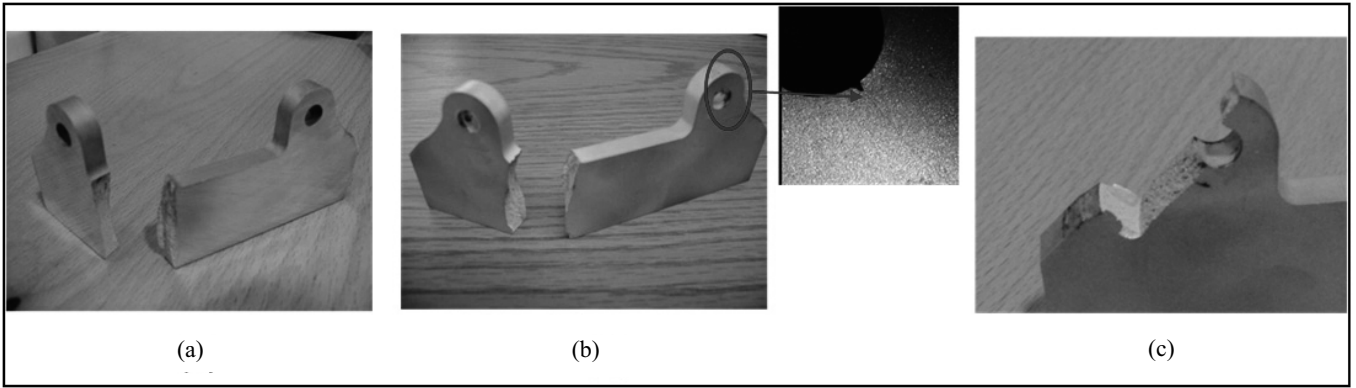


Figure 7. Failure modes of the lug joint samples under fatigue loading. (a) Polished sample, loading: (110lb – 1,100lb), (b) Sand blasted sample, loading: (110lb – 1,100lb), and (c) Sand blasted specimen, loading: (80lb – 800lb).

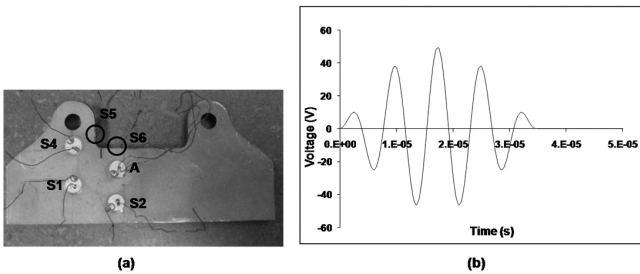


Figure 8(a). Sensor/actuator configuration for the lug joint sample, and (b) the excitation signal used.

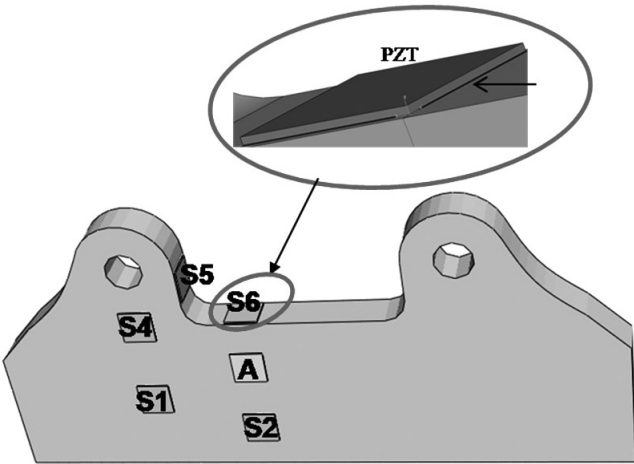


Figure 9. ABAQUS model of the lug joint sample instrumented with sensors/actuator.

Simulation of guided-waves propagating in an undamaged and damaged (4mm crack) lug joint sample was carried out using Abaqus/Explicit, a commercially available finite element software to perform dynamic simulations using explicit time integration. The lugs with sensors/actuator are modelled as an assembly of three different parts, viz lug, piezoelectric transducer, and adhesive layer. The lug is modelled as an isotropic, homogeneous, elastic material with properties typical of Al alloys, and continuum three dimensional brick elements (C3D8R) are used to mesh it. The mesh size varies for samples with different levels of crack (notch) lengths. Piezoelectric transducers are defined as orthotropic materials and are meshed with continuum three dimensional piezoelectric elements (C3D8E). The adhesive layer, which acts as the bonding between the

piezoelectric transducers and the lug joint sample, is modelled as a viscoelastic material and continuum three dimensional brick elements (C3D8R) are used to mesh it. The ABAQUS model of the lug joint sample is shown in Fig. 9.

Simulated results of the resultant displacement of guided-waves propagating in the lug joint sample are shown in Fig 10. It can be seen that the waves emanating from the actuator interact with the damage and are reflected back. Thus, a change is observed in the sensor signals from the damaged sample as compared to those for the undamaged case. This change in the sensor signals from the benchmark is further used to detect and characterise damage.

Frequency-domain studies are performed on the sensor signals simulated using finite element analysis. Figure 11 shows the magnitude of the Fourier transforms of the sensor signals. For clarity, only the region from 60KHz to 200KHz is shown since the dominant frequencies occur in this range. From the plots we see that damage causes a shift and attenuation of the spectral components in the signals for the healthy case. With the presence of a crack, the amplitude associated with a given dominant frequency (e.g. 220 at 138KHz) for the healthy sample attenuates to lower amplitudes (125 and 140) and occurs at two different frequencies (135KHz and 140KHz), respectively. This trend can also be seen in the case of 4mm crack length and is illustrated in the Table for the 138KHz frequency component.

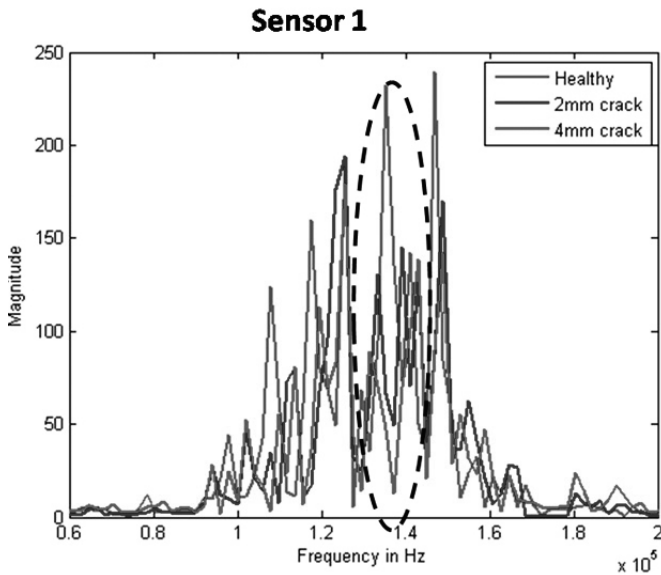
The frequency analysis for a given set of sensors at given locations contains information that can be used to characterise the nature of the crack, e.g., length and orientation. It is observed that localised changes in the dynamics of the system can influence the magnitude and phase of the frequency contents of each sensor signal with a given location. Hence this study is useful for defect characterisation once the sensor location is determined.

#### 4.0 DAMAGE ANALYSIS AND CLASSIFICATION USING TIME-FREQUENCY SIGNAL PROCESSING

This section examines time-frequency based damage classifiers<sup>(27-35)</sup>. The distinguishing feature of these algorithms is that they effect joint time-frequency analysis using the matching pursuit decomposition (MPD)<sup>(36)</sup>. The MPD is a versatile signal representation tool designed to yield not only high but also fully adaptive resolution in both time and frequency. This is a major advantage over other time-frequency techniques that have been investigated in the past, such as the multi-resolution wavelet transform<sup>(17)</sup>, which is capable of revealing temporal and spectral patterns in signals but is of limited utility when detecting small-scale damage requiring high frequency modes because of the drawback of low resolution in high frequency



Figure 10. Finite element simulation of the resultant displacement of guided-waves in the (a) healthy sample, and (b) damaged sample with 4mm crack.



**Sensor 1 (S1)**

Healthy		2mm crack		4mm crack	
Freq	Amp	Freq	Amp	Freq	Amp
		135	125	133	85
138	220				
		140	140	142	138

Figure 11. Frequency-domain comparison of sensor 1 signals obtained from modelling of different levels of damage in the lug joint.

regions<sup>(18)</sup>. The MPD has consequently been utilised in other detection problems also, such as target identification<sup>(37)</sup> and acoustic signal classification<sup>(38-40)</sup>.

For the purpose of damage classification, the MPD is used as a time-frequency representation (TFR) and feature extraction tool by projecting data onto a basis set composed of highly localised Gaussian functions. Classification is then carried out by matching features in the time-frequency plane based on statistics collected from available

training data. A somewhat direct approach<sup>(27,33)</sup> is to compute representative TFRs for each damage class of interest and classify data based on correlations in time-frequency space. Alternatively, the time-frequency features extracted using MPD can be modelled with stochastic modelling techniques, such as hidden Markov models (HMMs)<sup>(41,42)</sup>, and classification can then be performed in a Bayesian framework. In the following, our time-frequency based damage classification approach is described in more detail.

#### 4.1 Analysis with matching pursuit decomposition

The matching pursuit decomposition (MPD)<sup>(17,36)</sup> yields a representation for signals in terms of basis functions drawn from a redundant dictionary. The algorithm used for MPD iteratively decomposes a given signal  $s(t)$  as  $s(t) = \sum_{k=0}^{K-1} \alpha_k g_k(t) + R_K s(t) = s_K(t) + R_K s(t)$ , where  $R_K s(t)$  denotes the residue after  $K$  MPD iterations, and the expansion coefficients  $\alpha_k$  are given by the inner products between the residuals  $R_k s(t)$  and the dictionary atoms  $g_k(t)$ , which are selected so as to maximise the magnitude of the inner products at each step of the iteration. The truncation limit  $K$  is chosen such that the energy of the residue after  $K$  iterations is smaller than some pre-defined value. The procedure results in a compact 'best-fit' approximation  $s_K(t)$  in terms of the selected family of basis functions. The MPD algorithm can be implemented efficiently using the fast Fourier transform (FFT) with a computational complexity of  $O(N \log N)$ <sup>(36)</sup>, where  $N$  is the signal size.

The dictionary employed for MPD need not be orthonormal but is required to be complete<sup>(36)</sup>, and is customised based on specific components of interest in the signal class in question. The dictionary employed here is comprised of highly localised Gaussian atoms<sup>(36)</sup> of the form  $g_k(t) = e^{-\kappa_k^2(t-\tau_k)^2} \text{Cos}(2\pi\nu_k t)$ , where  $\tau_k$  is the time-shift,  $\nu_k$  is the frequency shift, and  $\kappa_k$  is the time-spread (scaling). The real Gaussian atoms are cosines of different frequencies and time shifts windowed by Gaussians with varying standard deviation. The Gaussian-windowed harmonics have advantages such as good time-frequency localisation properties and computational benefits derived from the availability of closed-form analytical expressions. Note that the MPD has been used with dictionary atoms composed of real measured data as well<sup>(30,33)</sup>, and the resulting decompositions have been shown to be extremely parsimonious. Each Gaussian atom  $g_k(t)$  is characterised by the set  $\{\tau_k, \nu_k, \kappa_k\}$ . The amplitude-time-frequency-scale features  $\{\alpha_k, \tau_k, \nu_k, \kappa_k\}_{k=0}^{K-1}$  extracted by the MPD encode the wave-physics necessary for distinguishing signals  $s_K(t) \approx s(t)$  from different damage classes.

The MPD can in addition be used to construct the cross-term free time-frequency representation (MPD-TFR), defined for the signal  $s_K(t)$

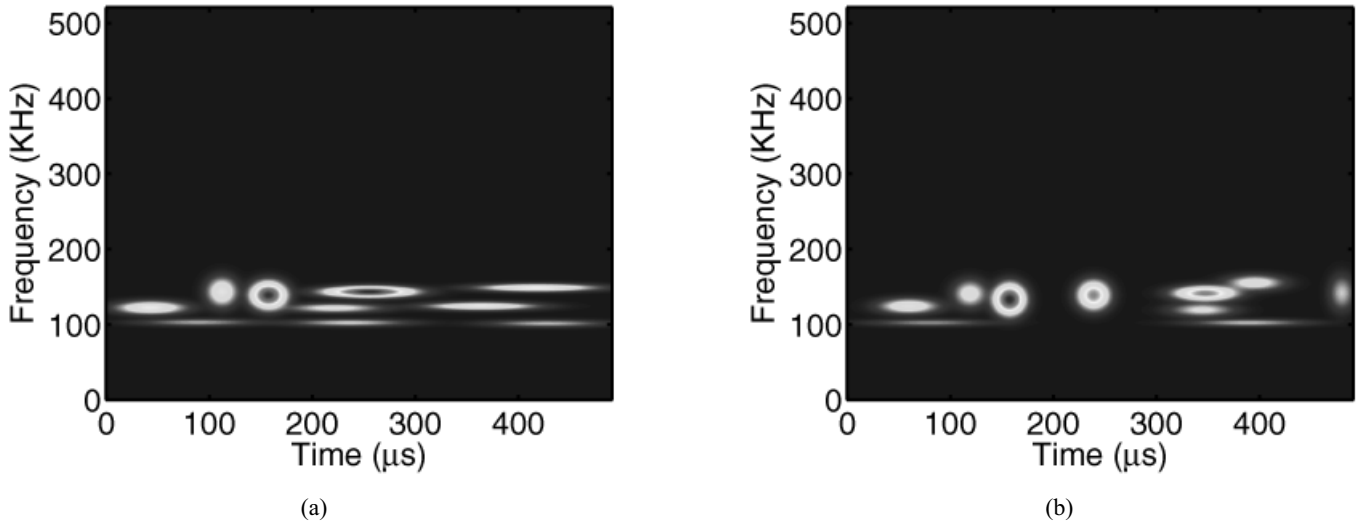


Figure 12. MPD-TFRs of data for an aluminum lug-joint sample (a) undamaged, and (b) with crack damage.

as<sup>(36)</sup>  $\mathcal{E}_{g_k}(t, f) \equiv \sum_{k=0}^{K-1} |\alpha_k|^2 \mathbf{W} \mathbf{D}_{g_k}(t, f)$ , where  $\mathbf{W} \mathbf{D}_{g_k}(t, f)$  is the Wigner distribution (WD)<sup>(16,18)</sup> of the atom  $g_k(t)$ . Figure 12 shows example MPD-TFRs of data for an aluminum lug-joint sample with and without crack damage. Note the marked difference in the time-frequency structure between the damaged and undamaged cases.

## 4.2 Hidden Markov model based damage classification

The hidden Markov model (HMM)<sup>(41,42)</sup> based damage classification approach<sup>(28,29)</sup> relies on the statistical characterisation of the time-frequency state dynamics of data from each damage class. Using the HMM, the time-frequency features extracted from structural data by the MPD are stochastically modelled as a Markov random process. A HMM is a probabilistic model used for modeling sequential data. Consider a length- $T$  observation sequence  $y = \{y_1, \dots, y_T\}$ . The HMM defines a probability distribution over  $y$  by invoking another sequence of unobserved (hidden) discrete variables  $x = \{x_1, \dots, x_T\}$  known as ‘states’. The model imposes (a) Markov dynamics on the sequence of hidden states, and (b) independence of the observations  $y_n$  from all other variables given  $x_n$ . Suppose that the number of distinct states is  $N$ , with the state variables  $x_n$  assuming values from the alphabet  $\{1, \dots, N\}$ . The model is then parameterised by the  $N \times 1$  initial state distribution vector  $\pi$  whose  $i$ th element is the probability  $p(x_1 = i)$ , the  $N \times N$  state-transition matrix  $\mathbf{A}$  whose  $(i, j)$ th element is  $p(x_{n+1} = j | x_n = i)$ , and the state-dependent observation density  $B$  whose  $j$ th element is  $b(y_n) = p(y_n | x_n = j)$ ; together the model parameters are denoted as the set  $\theta = \{\pi, \mathbf{A}, B\}$ . A graphical representation of a HMM is shown in Fig. 13.

For the purpose of damage classification, the observation sequences  $y = \{y_1, \dots, y_T\}$  are comprised of the four-dimensional vectors  $y_n = \{\alpha_n, \tau_n, \nu_n, \kappa_n\}$  of the extracted (time-ordered using time-shifts  $\tau_n$ ) MPD atoms (in a discrete HMM, the observations are quantised). The non-observable states  $x = \{x_1, \dots, x_T\}$  are defined as the regions of stationarity (regions in time where the frequency content remains close to constant) corresponding to the underlying physical dynamics of the damage wave physics. The HMM works by modelling the temporal transitions between these underlying states with a Markov random process in conjunction with the observation statistics. The features from each structural condition (damage class) are modelled with a separate HMM as the associated wave physics is different in each case.

The training data available from each damage class is used to learn the parameters of the corresponding HMM. Specifically, given the ‘training’ signals (observation sequences  $y$ ), an  $N$ -state HMM assumption is imposed and the maximum-likelihood (ML)<sup>(43,44)</sup> estimate of the parameters  $\theta$  is computed as  $\theta_{ML} = \operatorname{argmax}_{\theta} \operatorname{Log} p(y|\theta, N)$  using

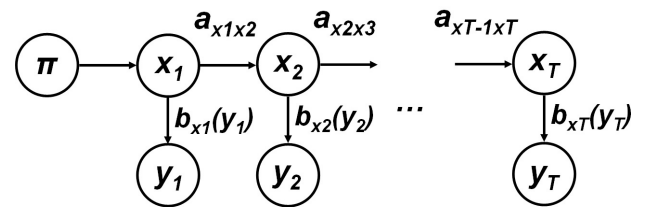


Figure 13. Graphical representation of a hidden Markov model.

the Baum-Welch algorithm<sup>(41,42)</sup>, a special case of the expectation-maximisation (EM) algorithm<sup>(43,44)</sup> which iteratively maximises the likelihood of the training data. The details of the HMM re-estimation procedure, relevant formulas, and complexity analysis can be found in Refs 34 and 42. Notably, all the relevant computations can be carried out with only  $O(N^2T)$  effort. Classification is then performed efficiently in a Bayesian framework<sup>(43,44)</sup>: a ‘test’ signal (observation sequence  $y'$ ) is classified to damage class  $m'$ , given by  $m' = \operatorname{argmax}_{m \in \{1, \dots, M\}} \operatorname{Log} p(y' | \theta_{ML}^m, N^m)$ , where  $\theta_{ML}^m$  and  $N^m$  denote the parameters and the number of states, respectively, of the HMM associated with the  $m$ th damage class.

## 4.3 Variational Bayesian learning for model selection

In the HMM training algorithm described above, the parameters  $\theta = \{\pi, \mathbf{A}, B\}$  are obtained as an ML point estimate  $\theta_{ML}$ . ML learning, however, provides no information about the uncertainty of the parameters estimated. In some cases, the ML point estimate may be unrepresentative of the true posterior. Moreover, as is well known<sup>(44)</sup>, ML learning does not account for model complexity and is susceptible to over-fitting the data. The likelihood function is unbounded and it is possible to increase the likelihood of the data by using models of increasing complexity. Using ML learning with unnecessarily complex models is therefore undesirable, and has the disadvantages of increased data requirement and computational burden.

Conventional methods for dealing with this problem include restricting the model complexity by limiting the number of model parameters (which, in the present context, is governed by the number of HMM states  $N$ ), constraining the form and information-flow in the model (for example, by constraining the connectivity of the state-transition matrix  $\mathbf{A}$ ), using maximum *a posteriori* (MAP)<sup>(44)</sup> learning with regularising priors on the parameters, and employing cross-validation. These techniques work well in some applications, but often they become cumbersome and/or computationally expensive.

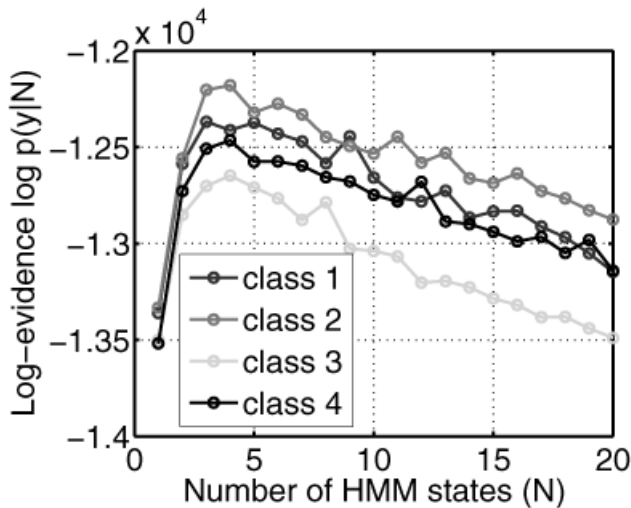


Figure 14. Lower bound  $\mathcal{F}_N^*$  on the log-evidence  $\text{Log } p(y|N)$  for the training signals as a function of number of HMM states  $N$ .

This work follows the Bayesian approach to the task of model selection by calculating the posterior distribution over the number of HMM states  $N$  given the data  $y$  and *a priori* knowledge  $p(N)$  (assumed uniform). Specifically, models are ranked by evaluating the evidence  $p(y|N)$ , which has the advantage of automatically penalising complex models with more parameters<sup>(44)</sup>.

Variational Bayesian (VB) learning<sup>(44,45)</sup> provides an efficient framework for the evaluation of the evidence  $p(y|N)$ . In the VB learning for determining the number of HMM states  $N$ , the evidence is lower bounded with a variational objective function  $\mathcal{F}_N$  by making use of the Kullback-Leibler (KL) divergence<sup>(44)</sup>. The variational Bayesian EM (VBEM) algorithm<sup>(45)</sup> iteratively maximises the bound  $\mathcal{F}_N$  and convergence is guaranteed to a local maximum  $\mathcal{F}_N^*$ . The optimal number of states  $N^*$  is determined by comparing the evidences for various states as  $N^* \approx \text{argmax}_N \mathcal{F}_N^*$ . The relevant update equations for VB HMMs can be found in Refs 45 and 46. It is important to note that the advantages of the VB learning are afforded at a computational cost that is not very different from that of the standard EM algorithm<sup>(45,46)</sup>.

#### 4.4 Classification of crack damage in an aluminium lug-joint

The problem of classifying crack damage in an aluminium lug-joint sample is now considered. Fatigue testing was performed on 6.35mm (0.25in) thick polished Al 2024 T351 lug-joint samples. The lugs are subjected to tension-tension loading of 423 – 4,230N (95 – 950lb) at 20Hz. Surface-mounted piezoelectric sensors are used to actuate and measure response to a tone-burst signal of central frequency 130KHz. Sensor data was recorded for four different structural conditions (damage classes): Class 1 (unfatigued lug joint), Class 2 (lug joint fatigued to 120 kilo-cycles), Class 3 (lug joint fatigued to 200 kilo-cycles), and Class 4 (lug joint fatigued to 340 kilo-cycles). Altogether, 1,600 signals are collected from two samples (400 for each damage class).

The time-frequency discrete HMM based damage classifier is employed for this problem. Time-frequency feature extraction is first performed on the data using  $K = 15$  iterations of MPD with a dictionary composed of about 16m Gaussian atoms. This choice of  $K$  corresponds to a residual signal energy of 10%. The resulting MPD features are discretised using vector quantisation with 256 codes (the number of codes is estimated by testing the classifier performance on 100 validation signals from each class). Figure 14 shows a plot of the lower bound  $\mathcal{F}_N^*$  on the log-evidence  $\text{Log } p(y|N)$  for 200 training signals (for each class) computed using VB learning as a function of the number of

**Table 2**  
Confusion matrix for classification of fatigue damage in an aluminum lug joint using the time-frequency discrete HMM based damage classifier

	Class 1	Class 2	Class 3	Class 4
Class 1	0.85	0.02	0.12	0.01
Class 2	0.04	0.92	0.02	0.02
Class 3	0.05	0.01	0.94	0.00
Class 4	0.01	0.00	0.00	0.99

**Table 3**  
Average correct classification rates as a function of number of codes used in the time-frequency discrete HMM based damage classifier

# codes	mean $p_{ii}$
64	0.82
128	0.86
256	0.93

HMM states  $N$ . It is observed that the evidence is generally greatest for  $N = 2$  to 5 state HMMs, and decreases as  $N$  is increased further (i.e., with increasing model complexity).  $N = 3$ -state discrete HMMs are consequently used to model the data from each of the four damage classes. The parameters  $\theta$  of each HMM are estimated from 200 training signals using 20 iterations of the Baum-Welch algorithm. The performance of the classifier is finally tested using 100 test signals from each damage class.

The classification results are shown here with the help of a confusion matrix (Table 2). The  $(i, j)$ th entry of a confusion matrix indicates the probability  $p_{ij}$  that data actually from class  $i$  is classified as belonging to class  $j$ . The diagonal entries  $p_{ii}$  are therefore the probabilities of correct classification. From the results shown in Table 2, it can be seen that the performance of the time-frequency HMM based damage classifier is good (the average correct classification rate is about 93%). It should be noted that, to a limited extent, these results incorporate the effects of sample variability.

It is observed that the classifier performance is weakest for Class 1. This is explained by examination of the MPD-TFRs, which reveals that Class 1 data shows similar time-frequency structure to Class 3 data and is consequently misclassified often to Class 3 as seen in the confusion matrix. The authors' own experience with various SHM scenarios suggests that the data for the undamaged case is usually distinct from — and shows less variability than — that for the damaged cases, but not always. Note that in all cases a different HMM is used to model data from each class; the similarity arguments (and the confusion matrices) are not symmetric.

The performance of the discrete HMM classifier also depends on the number of codes used for quantisation. The larger the number of codes, the smaller the information loss due to quantisation, and the better the performance. The classification results reported in Table 2 are obtained using 256 codes and (at added computational cost) can be improved further by increasing the number of codes. Table 3 shows the performance of the discrete HMM classifier as a function of the number of codes. We can see that the average correct classification rate improves as the number of codes is increased. Alternatively, continuous HMM based damage classifiers<sup>(29,34)</sup> can be employed.

In order to study the classification algorithm's performance in the presence of noise, simulated data generated from FEM analysis is utilised to establish a noise-free baseline. A three-dimensional finite element modelling (FEM) is carried out for a 6.35mm (0.25in) thick Al 2024-T3 alloy plate with a polished surface finish using the commercial finite element software Abaqus/Explicit. Two surface-mounted piezoelectric sensors (one transmitter and one receiver) are incorporated in the model. A tone burst signal of central frequency

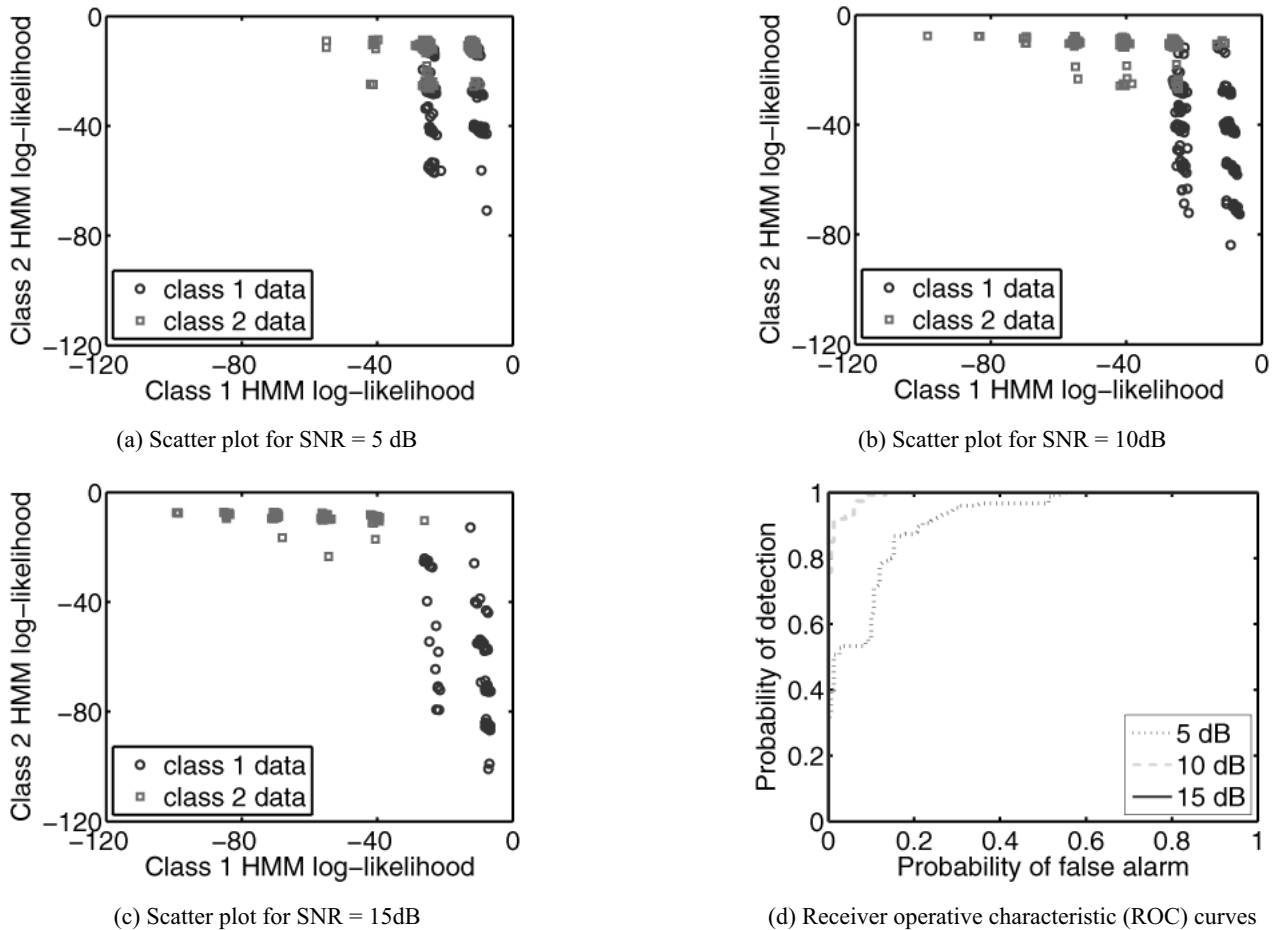


Figure 15. Scatter plots and receiver operative characteristic (ROC) curves for different SNRs (Class 1: undamaged lug-joint, Cass 2: lug-joint with 4mm crack damage).

130KHz is used as the actuation. Response signals are computed for two damage classes: Class 1 (undamaged sample), and Class 2 (sample with 4mm crack). Since the data from the physics-based model is deterministic but the classification methods are stochastic (and rely on training data that accounts for variability), a dataset of 900 signals (450 for each class) is generated by adding controlled amounts of white Gaussian noise to the response signals.

Time-frequency discrete HMM based damage classification is carried out as before. Feature extraction is performed on the data using  $K = 10$  iterations of MPD with a dictionary composed of 33m Gaussian atoms. The resulting MPD features are discretised using vector quantisation with 16 codes (the number of codes is estimated by testing the classifier performance on 150 validation signals from each class).  $N = 3$ -state discrete HMMs are used to model the data from each of the two damage classes. The parameters  $\theta$  of each HMM are estimated from the 150 training signals using 30 iterations of the Baum-Welch algorithm. The performance of the classifier is finally tested using 150 test signals from each damage class. In order to test the performance of the classifier in the presence of noise, the HMMs are trained and validated on relatively noise-free data with signal-to-noise ratio (SNR) = 20dB and tested using data with high, moderate, and low amounts of noise (SNR = 5, 10, and 15dB, respectively).

Figures 15(a)-(c) show scatter plots of the log-likelihoods of the data computed by the HMM associated with each class, for SNR = 5, 10, and 15dB, respectively. It is seen that, as expected, the data from a class receives a higher likelihood value from the HMM associated with that class than from the HMM associated with another class. Furthermore, as the SNR increases (corresponding to a decrease in noise levels), the

separation between the data from the different damage classes becomes clearer. Figure 15(d) quantifies these observations in the form of receiver operating characteristic (ROC) curves, showing the probability of detection computed as a function of the probability of false alarm, for the different SNR levels. In general, higher detection probabilities are associated with a higher false alarm rates. Observe in addition that for any given false alarm rate, larger SNR values yield higher detection probabilities. From the plot, it can be seen that the probability of correctly detecting the damage is high for SNR = 10dB and 15dB (even at very low false alarm rates) and fair for SNR = 5dB, indicating a robust and reliable damage classification performance.

The corresponding confusion matrices are shown in Table 4. Also provided here are the 95% confidence intervals on the classification probabilities  $p_{ij}$ . The probabilities and the intervals are estimated using the fact that the posterior over  $p_{ij}$  is Beta distributed (assuming a uniform prior). From the tables, it is seen that the performance of the classifier is very good for SNR = 10 and 15dB (with average correct classification probabilities greater than 90%) and fair for SNR = 5dB.

## 5.0 PROGNOSIS WITH PREDICTIVE MODELS

A hybrid prognosis model is developed based on both physics and data driven techniques. A schematic of the hybrid prognosis model is shown in Fig. 16.

The overall prognosis model has three different modules: an offline physics-based module for baseline signal features and deterministic

**Table 4**  
Confusion matrices for different SNRs, with 95% confidence intervals (Class 1: undamaged lug-joint, Class 2: lug-joint with 4mm crack damage)

	Class 1	Class 2
Class 1	0.84 ± 0.06	0.16 ± 0.06
Class 2	0.16 ± 0.06	0.84 ± 0.06
(a) SNR = 5dB		
	Class 1	Class 2
Class 1	0.91 ± 0.04	0.09 ± 0.04
Class 2	0.02 ± 0.02	0.98 ± 0.02
(b) SNR = 10dB		
	Class 1	Class 2
Class 1	0.97 ± 0.03	0.03 ± 0.03
Class 2	0.01 ± 0.01	0.99 ± 0.01
(c) SNR = 15dB		

residual life estimation, an offline data-driven module<sup>(47)</sup> for probabilistic residual life estimation and an online state-estimation module<sup>(48)</sup> for real-time damage state estimation. All three sub-modules are finally integrated to develop a hybrid prognostic model. The offline physics-based model is based on a micro-meso-macro multiscale model, whereas the offline data-driven model and the online state estimation model are based on a Gaussian process approach with Bayesian inference<sup>(49,50)</sup>. The offline data-driven model implicitly models the macro-level uncertainty that arises due to microstructure variability, loading uncertainty, etc., and complements the offline physics-based model for uncertainty in damage propagation and for any unmodelled exogenous influences. The physics-based model combined with a data-driven probabilistic model are used for offline prediction of residual useful life, whereas an online predictive model based on piezoelectric sensor signals estimates the current damage state in real-time using Gaussian process modeling and makes this information available to the offline module to reassess the residual useful life of the structural components based on the real-time information. The present work will focus on the offline data driven prognostics/forecasting model and the online state estimation model and their integration to estimate the residual useful life in real-time.

Based on the extracted signal features, the Gaussian process algorithm is used to assess the corresponding damage state of the hotspot. The Gaussian process input and output space are respectively trained with signal features and crack length data from one sample (sample-203). The online state estimation algorithm is then tested on another sample (sample-202). The input space for both the training sample and test sample are fed with four types of signal features: resonant frequency based features from sensors S3 and S4, and signal variance based feature from sensors S3 and S4. However, it should be noted that unlike the Gaussian process training input space, the test input space is fed with features, as they become available, in real-time. The test output at a typical fatigue cycle has to be predicted using the  $4 \times 1$  feature vector extracted at that fatigue cycle. The comparison between predicted damage state (crack length) and the experimental value is depicted in Fig 17. From the figure, it can be seen that there is a good correlation between the experiment and the prediction, when the crack length is larger than 5mm. The discrepancy between prediction and experiment increases as the crack length becomes smaller. This is possibly because the signal features are not sensitive enough to smaller damage conditions, i.e., shorter crack lengths. This problem can be solved by using high frequency input signals and nonlinear feature extraction techniques, which will be addressed in the future.

The estimated online damage states are finally fed into a prognosis model, to forecast the residual life of the structural hotspot. As mentioned earlier, the prognosis model is also a probabilistic model based on the Gaussian process approach. For the offline forecasting model the future mean and variance of the damage state rate is

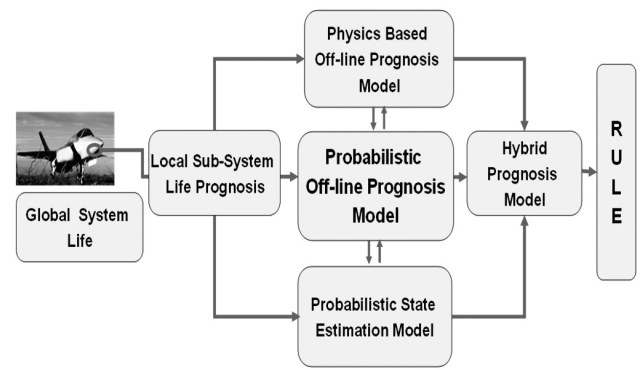


Figure 16. A conceptual hybrid prognostic model (source of the fighter plane image: <http://www.jsf.mil>).

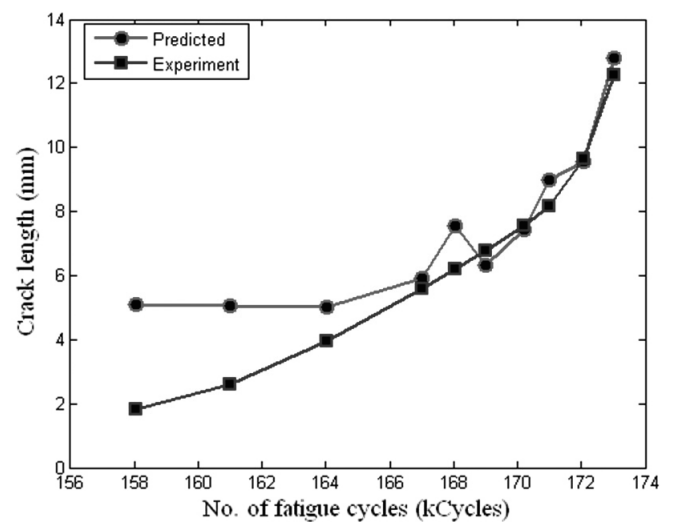


Figure 17. Online damage state estimation from sensor signal features.

predicted. It is known from linear elastic fracture mechanics that the crack growth rate at a future fatigue cycle ( $(L+\Delta L)$ th cycle) is a function of the stress intensity range, or, in other words, a function of the future cycle ( $(L+\Delta L)$ th cycle) minimum load, maximum load, and the current cycle ( $L$ th cycle) damage condition or crack length. From this physical concept, the Gaussian process function mapping can be performed between inputs: ( $L + \Delta L$ )th cycle loading information and  $L$ th cycle damage condition, and the output: the ( $L+\Delta L$ )th cycle crack growth rate. The Gaussian technique based prognosis model is a multivariate mapping process, and many variables that affect damage can be fed into it. However, for the crack growth estimation results shown in Fig 18, only  $L$ th cycle damage state information (crack length) is introduced into the Gaussian process input space. Loading information is not introduced into the Gaussian process input space since the loading has constant amplitude and statistically leads to a stationary ergodic process. However, it should be noted that for spectrum loading it is necessary to include the loading information to the Gaussian process input space (in addition to the  $L$ th cycle damage state information). This would help the Gaussian process model to effectively map the transient and load interaction effect to the output damage state in the case of real-life spectrum loading. For the present case, the  $L$ th cycle crack length predicted from the online state estimation model is the only parameter fed to the offline prognosis model input space to forecast the ( $L + \Delta L$ )th cycle damage state. Once the ( $L+\Delta L$ )th cycle fatigue crack growth rate is predicted, linear integration is performed to estimate the crack length at the ( $L+\Delta L$ )th cycle.

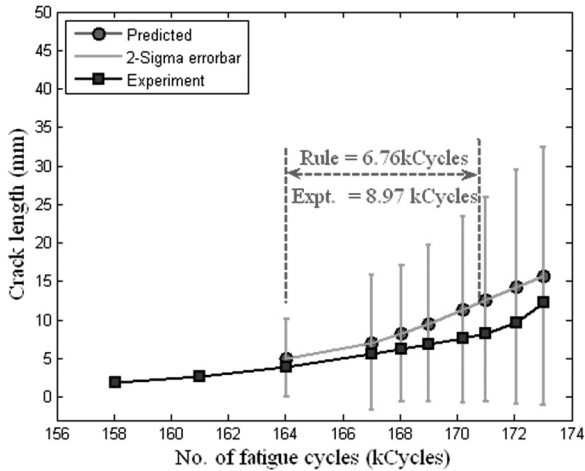


Figure 18. Residual useful life estimate for sample-202.

The estimated crack length is then fed back to the Gaussian process offline module to predict the rate at a future fatigue cycle, and using this new predicted rate the corresponding new crack length is estimated. The offline prediction is continued until the critical crack length of the component is reached. The difference between the number of cycles at which the offline model estimated crack length becomes critical and the number of cycles at which the last online damage state information was available, gives the residual useful life estimation (RULE) of the component. A typical result showing RULE, with online damage state information available at 164 kilo-cycles, is shown in Fig. 18. Note that the online state estimation is performed in an outer loop (called the structural health monitoring loop), in which continuous damage state information is inferred from the piezoelectric sensor signals and fed into the inner offline prognosis loop. The outer online and inner offline loops continue to run as long as the component survives failure or is allowed to retire. Figure 19 shows the mean square error between forecasted crack length and that found from experiment. The individual fatigue cycles, where the error bars are shown, correspond to those up to which the online predicted crack growth data are available. The predicted crack growth data are not necessarily the same as the real crack growth data found using the high-resolution camera. Also, it is seen from Fig. 19 that as more online data are available there is a clear trend in reduction of the mean square error. The slight discrepancies at 169 kilo-cycles and 171 kilo-cycles are possibly due to accumulated error caused by the error in online state estimation. It can be seen from Fig. 17 that there is a discrepancy between online prediction and experiment at 168 kilo-cycles and 171 kilo-cycles. The mean square error can be further reduced by providing a large amount of offline data for training the Gaussian process model.

## 6.0 CONCLUSION

A physically-based multiscale model has been developed in this paper for fatigue damage analysis. The results show that size and orientation effects at the micro level have a significant impact on wave and damage interaction. Single crystal plasticity serves as the foundation for the mesoscale modelling applied to each grain. Macroscale analysis was accomplished by using a multiscale framework, i.e., using the average stress-strain response from the mesoscale to describe the material behaviour outside the critical location and a microscale model to describe the material behaviour within the critical site area. It is found that owing to sample geometry, grain orientation and size, the stress distribution is not homogenised in the critical area. The use of different realisations of the microstructural representation at the critical site can be used to generate statistics of damage accumulation variability.

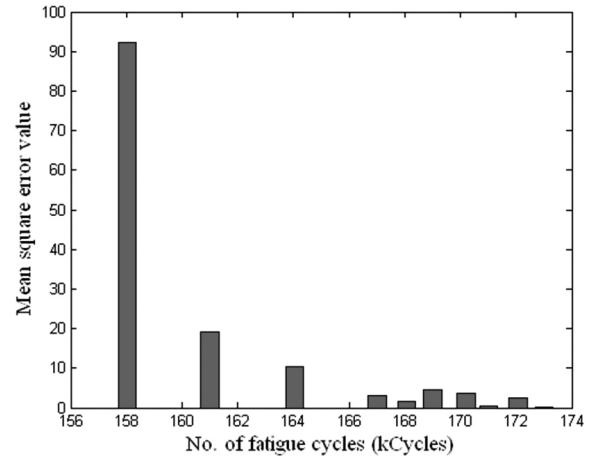


Figure 19. Mean square error between estimated crack growth and experimental results at different fatigue cycles.

The detection of fatigue-induced damage in a structural hotspot (lug joint) was investigated. Finite element analysis carried out with piezoelectric wafers bonded to the host structure was used to simulate sensor signals. Guided-wave propagation studies were performed to characterise structural defects, with analysis showing sensitivity of the signals to the presence of damage.

Time-frequency techniques have been proposed for damage classification. The approach relies on extracting amplitude-time-frequency-scale features from structural data using the matching pursuit decomposition (MPD) with highly localised Gaussian functions. Classification is performed by matching features in the time-frequency plane and by stochastic modeling of the features using hidden Markov models (HMMs) with Bayesian inference. Statistics are collected from available training data. The HMM based damage classifier is adapted for real-time use by using variational Bayesian learning to estimate the number of HMM states  $N$  automatically from the data. The damage classification method is tested on modelled data for the lug joint and very high rates of correct classification (near 90%) are observed. Examination of the algorithm's performance in the presence of noise shows promising results and confirms the robustness of the approach.

An adaptive online-offline life prediction model has been developed to estimate the residual life of structural hotspots in real-time. Both the online and offline models are based on a Gaussian process approach utilising probabilistic Bayesian inference. The online-offline prognostic model is validated on a structural hotspot, here, an Al 2024-T351 lug joint. Once the current damage state is predicted, it is fed to the Gaussian process based offline forecasting model to estimate the residual useful life (RUL) based on the new damage information available. The offline forecasting model is a probabilistic mapping between the current crack state (input), and the future crack growth rate (output). It is found that there is a good correlation between the residual life estimation from the online-offline prognostic model and actual experiments. It is also found that the error between the forecasted crack length and the real (experimental) crack length reduces as more online data are available to the prognostic model.

## ACKNOWLEDGMENTS

This research was supported by the DoD AFOSR Grant FA9550-06-1-0309 (Program manager: Dr Victor Giurgiutiu). The authors would like to acknowledge team members: Chuntao Luo, Sunilkumar Soni, Debejoy Chakraborty, Wenfan Zhou, Subhasish Mohanty, Manuel Parra-Garcia, and Jun Wei. Special thanks to the reviewers for comments that helped improve the document.

## REFERENCES

1. FARRAR, C.R. and WORDEN, K. An introduction to structural health monitoring, 2007, *Phil Trans R Soc A*, **365**, pp 303–315.
2. FARRAR, C.R. and LIEVEN, N.A.J. Damage prognosis: the future of structural health monitoring, *Phil Trans R Soc A*, 2007, **365**, pp 623–632.
3. STASZEWSKI, W.J., BOLLER, C. and TOMLINSON, G.R. *Health Monitoring of Aerospace Structures*, 2003, Wiley, UK.
4. Production processes, United States Air Force Scientific Advisory Board, 1992, Report of the AdHoc Committee on Air Force Aircraft Jet Engine Manufacturing and SAF/AQQS: Pentagon, Washington, DC, USA.
5. LEMAITRE, J. and DESMORAT, R. *Engineering Damage Mechanics*, 2005, Springer, Berlin, Heidelberg, New York.
6. SONI, S., DAS, S. and CHATTOPADHYAY, A. Simulation of damage-features in a lug joint using guided waves, *J Intelligent Material Systems and Structures*, August 2009, **20**, pp 1451–1464.
7. SONI, S., BANERJEE, S., DAS, S. and CHATTOPADHYAY, A. Simulation of damage-features in complex joint using guided waves, 2008, Proc SPIE Smart Structures and Materials and Nondestructive Evaluation and Health Monitoring, San Diego, California, invited Session on Information Management for Structural Health Monitoring.
8. SONI, S., DAS, S. and CHATTOPADHYAY, A. Guided wave based technique for optimal sensor placement and damage detection, 2009, Proc 50th AIAA/ASME/ASCE/AHS/ASC Structures, Structural Dynamics and Materials Conference, Palm Springs, California.
9. SONI, S., DAS, S. and CHATTOPADHYAY, A. Sensor sensitivity studies to monitor crack growth in lug joint structures, 2009, Proc SPIE Smart Structures and Materials and Nondestructive Evaluation and Health Monitoring, San Diego, California.
10. DALTON, R.P., CAWLEY, P. and LOWE, M.J.S. The potential of guided waves for monitoring large areas of metallic aircraft fuselage structure, *J Nondestructive Evaluation*, 2001, **20**, pp 29–46.
11. LEE, B.C. and STASZEWSKI, W.J. Modelling of Lamb waves for damage detection in metallic structures: Part I — Wave propagation, *Smart Mater Struct*, 2003, **12**, pp. 804–814.
12. EREN, L. and DEVANEY, M.J. Bearing damage detection via wavelet packet decomposition of the stator current, *IEEE Transactions on Instrumentation and Measurement*, 2004, **53**, pp 431–436.
13. PARK, G., RUTHERFORD, A.C., SOHN, H. and FARRAR, C.R. An outlier analysis framework for impedance-based structural health monitoring, *J Sound and Vibration*, 2005, **286**, pp 229–250.
14. SOHN, H., ALLEN, D.W., WORDEN, K. and FARRAR, C.R. Structural damage classification using extreme value statistics, *J Dynamic Systems, Measurement, and Control*, 2005, **127**, pp 125–132.
15. LEE, J.W., KIRIKERA, G.R., KANG, I., SCHULZ, M.J. and SHANOV, V. N., Structural health monitoring using continuous sensors and neural network analysis, *Smart Mater Struct*, 2006, **15**, pp 1266–1274.
16. COHEN, L. Time-frequency distributions — A review, *Proceedings of the IEEE*, 1989, **77**, pp 941–981.
17. MALLAT, S.G. *A Wavelet Tour of Signal Processing*, Second edition, 1998, Academic Press.
18. PAPANDREOU-SUPPAPPOLA, A. (Ed). *Applications in Time-Frequency Signal Processing*, 2002, CRC Press, Florida.
19. LUO, C., WEI, J., GARCIA, M., CHATTOPADHYAY, A. and PERALTA, P. A multiscale model for fatigue damage prediction in metallic materials, 2008, 49th AIAA/ASME/ASCE/AHS/ASC Structures, Structural Dynamics and Materials Conference, Schaumburg, Illinois.
20. HILL, R. Generalized constitutive relations for incremental deformation of metal crystals by multislip, *J Mech Phys Solids*, 1966, **14**, p 95.
21. RICE, J.R. Inelastic constitutive relations for solids: An internal-variable theory and its application to metal plasticity, *J Mech Phys Solids*, 1971, **19**, p 433.
22. HILL, R. and RICE, J.R. Constitutive analysis of elastic-plastic crystals at arbitrary strain, *J Mech Phys Solids*, 1972, **20**, p 401.
23. ASARO, R.J. and RICE, J.R. Strain localization in ductile single crystals, *J Mech Phys Solids*, 1977, **25**, p 309.
24. ASARO, R.J. Micromechanics of crystals and polycrystals, *Adv Appl Mech*, 1983, **23**, p 1.
25. ASARO, R.J. Crystal plasticity, *J Appl Mech*, 1983, **50**, p 921.
26. JIANG, Y. A fatigue criterion for general multiaxial loading, *Fat Frac Eng Mat Struct*, 2000, **23**, p 19.
27. KOVVALI, N., DAS, S., CHAKRABORTY, D., COCHRAN, D., PAPANDREOU-SUPPAPPOLA, A. and CHATTOPADHYAY, A. Time-frequency based classification of structural damage, 2007, 48th AIAA/ASME/ASCE/AHS/ASC Structures, Structural Dynamics, and Materials Conference, pp 2047–2055, Honolulu, Hawaii.
28. ZHOU, W., KOVVALI, N., PAPANDREOU-SUPPAPPOLA, A., COCHRAN, D. and CHATTOPADHYAY, A. Hidden Markov model based classification of structural damage, Proc of SPIE, 2007, **6523**, p 652311.
29. ZHOU, W., CHAKRABORTY, D., KOVVALI, N., PAPANDREOU-SUPPAPPOLA, A., COCHRAN, D. and CHATTOPADHYAY, A. Damage classification for structural health monitoring using time-frequency feature extraction and continuous hidden Markov models, 2007, Asilomar Conference on Signals, Systems, and Computers, pp 848–852, Pacific Grove, California.
30. CHANNELS, L., CHAKRABORTY, D., SIMON, D., KOVVALI, N., SPICER, J., PAPANDREOU-SUPPAPPOLA, A., COCHRAN, D., PERALTA, P. and CHATTOPADHYAY, A. Ultrasonic sensing and time-frequency analysis for detecting plastic deformation in an aluminum plate, *Proc of SPIE*, 2008, **6926**, p 69260P.
31. CHAKRABORTY, D., SONI, S., WEI, J., KOVVALI, N., PAPANDREOU-SUPPAPPOLA, A., COCHRAN, D. and CHATTOPADHYAY, A. Physics based modeling for time-frequency damage classification, *Proc of SPIE*, 2008, **6926**, p 69260M.
32. ZHOU, W., REYNOLDS, W.D., MONCADA, A., KOVVALI, N., CHATTOPADHYAY, A., PAPANDREOU-SUPPAPPOLA, A. and COCHRAN, D. Sensor fusion and damage classification in composite materials, *Proc of SPIE*, 2008, **6926**, p 69260N.
33. CHAKRABORTY, D., KOVVALI, N., WEI, J., PAPANDREOU-SUPPAPPOLA, A., COCHRAN, D. and CHATTOPADHYAY, A. Damage classification for structural health monitoring using timefrequency techniques, *J Intelligent Material Systems and Structures*, Special issue on Structural Health Monitoring, July 2009, **20**, pp 1289–1305.
34. ZHOU, W., KOVVALI, N., PAPANDREOU-SUPPAPPOLA, A., COCHRAN, D., CHATTOPADHYAY, A. and REYNOLDS, W. Classification of damage in composite structures using hidden Markov models for integrated vehicle health management, *J Intelligent Material Systems and Structures*, Special issue on Structural Health Monitoring, July 2009, **20**, pp 1271–1288.
35. CHAKRABORTY, D., ZHOU, W., SIMON, D., KOVVALI, N., PAPANDREOU-SUPPAPPOLA, A., COCHRAN, D. and CHATTOPADHYAY, A. Time-frequency methods for structural health monitoring, 2008, Sensor, Signal and Information Processing (SenSIP) Workshop.
36. MALLAT, S.G. and ZHANG, Z. Matching pursuits with time-frequency dictionaries, *IEEE Transactions on Signal Processing*, 1993, **41**, pp 3397–3415.
37. BHARADWAJ, P.K., RUNKLE, P. and CARIN, L. Target identification with wave-based matched pursuits and hidden Markov models, *IEEE Transactions on Antennas and Propagation*, 1999, **47**, pp 1543–1554.
38. EBENEZER, S.P. Classification of Time-varying Signals from an Acoustic Monitoring System using Time-frequency Techniques, December 2001, Master's thesis, Arizona State University, Tempe, AZ.
39. EBENEZER, S.P., PAPANDREOU-SUPPAPPOLA, A. and SUPPAPPOLA, S.B. Matching pursuit classification for time-varying acoustic emissions, 2001, 35th Asilomar Conference on Signals, Systems and Computers, pp 715–719.
40. EBENEZER, S.P., PAPANDREOU-SUPPAPPOLA, A. and SUPPAPPOLA, S.B. Classification of acoustic emissions using modified matching pursuit, *EURASIP J Applied Signal Processing*, 2004, **3**, pp 347–357.
41. RABINER, L.R. and JUANG, B.H. An introduction to hidden Markov models, *IEEE ASSP Magazine*, 1986, pp 4–15.
42. RABINER, L.R. A tutorial on hidden Markov models and selected applications in speech recognition, 1989, Proceedings of the IEEE, **77**, pp 257–286.
43. DUDA, R.O., HART, P.E. and STORK, D.G. *Pattern Classification*, Second edition, 2001, Wiley Interscience.
44. MACKAY, D.J.C. *Information Theory, Inference, and Learning Algorithms*, 2003, Cambridge University Press.
45. BEAL, M.J. Variational Algorithms for Approximate Bayesian Inference, 2003, PhD thesis, Gatsby Computational Neuroscience Unit, University College London.
46. MACKAY, D.J.C. Ensemble learning for hidden Markov models, 1997, Technical report, Cavendish Laboratory, University of Cambridge.
47. MOHANTY, S., DAS, S., CHATTOPADHYAY, A. and PERALTA, P. Gaussian process time series model for life prognosis of metallic structure, *J Intelligent Material Systems and Structures*, to appear.
48. MOHANTY, S., CHATTOPADHYAY, A., PERALTA, P., DAS, S. and WILLHAUCK, C. Fatigue life prediction using multivariate Gaussian process, 2008, AIAA/ASME/ASCE/AHS/ASC Structures, Structural Dynamics and Materials Conference, Schaumburg, Illinois, 2008.
49. MACKAY, D.J.C. Introduction to Gaussian processes, *Neural Networks and Machine Learning*, BISHOP, C.M. (Ed), 1998, pp 133–165, Springer, Berlin.
50. RASMUSSEN, C. and WILLIAMS, C. *Gaussian Processes for Machine Learning*, 2006, The MIT Press, Cambridge, MA, USA.